Nanoscale

PAPER

View Article Online
View Journal | View Issue

Cite this: *Nanoscale*, 2024, **16**, 22201

Stretchable photosensors with InN nanowires operating at a wavelength of 1.3 µm

Jaehyeok Shin, Siyun Noh, Seunghwan Jhee, Sumin Kang, Yumin Lee and Jin Soo Kim *

Received 8th August 2024,
Accepted 30th October 2024

DOI: 10.1039/d4nr03257h

rsc.li/nanoscale

Stretchable photosensors, which operate in the wavelength window of 1.3 µm, were fabricated with InN nanowires (NWs) and graphene to serve as a light-absorbing medium and carrier channel, respectively. Specifically, the stretchable photosensors were fabricated by transferring InN NWs embedded in graphene layers onto polyurethane substrates pre-stretched at the strain levels of 10, 20, 30, 40, 50, and 60%. An InN-NW photosensor fabricated at the pre-strain level of 50% and stretched at the strain of 50% produces a photocurrent of 0.144 mA, which corresponds to 76.2% of that (0.189 mA) measured in the released state. The photocurrent and photoresponsivity of the photosensor measured after 1000 cyclic-stretching tests are comparable to those measured before stretching. The performance of the stretchable photosensors was largely unaffected by parameters such as the relative humidity and duration of operation (up to 30 days), indicating that the devices operate very stably.

Introduction

A photosensor operating at a wavelength of 1.3 µm is one of the core components of optical communication systems. In particular, a photosensor should be highly sensitive with low noise and fast response characteristics to be suitable for wavelength division multiplication applications in local and metropolitan networks.[1–3] Recently, the new concept of a light-fidelity (Li-Fi) system has been proposed for next-generation short-range wireless communication that would not only be able to transmit large amounts of information faster than a wireless-fidelity method, but would also offer high security.[4,5] Additionally, for Li-Fi systems, a photosensor operating at the wavelength of 1.3 µm is very important from the perspective of eye safety. To effectively transmit or receive optical communication using the Li-Fi system, the devices must be attached to the human body or machines. In view of this, to effectively implement attachable or wearable devices, the individual components ultimately should have stretchable characteristics beyond flexible characteristics.[6] That is, the superior mechanical stretchability of devices with reliable performance and good durability is required to realize the attachable and wearable systems. For personalized optical communication systems, for example, it is better that photosensors are stretchable. Commercially available photosensors operating at a wavelength of 1.3 µm largely use InGaAs and InGaAsP as the photosensor. Kozyreva *et al.* reported a high-speed 1.3 µm photosensor based on an InGaAs thin film.[1] However, semiconductor thin films are not inherently flexible, and few flexible or stretchable devices have been reported. Lee *et al.* reported a flexible photosensor fabricated with the polymer materials of poly(triarylamine) and poly[*N*,*N*′-bis(4-butylphenyl)-*N*,*N*′-bis(phenyl)benzidine].[7] However, the photocurrent generated by their device was as weak as 30 nA, which would need to be improved for practical applications. More recently, hybrid organic–inorganic, inorganic, and organic materials such as metal–organic frameworks, perovskites, and conductive polymers were also used for the fabrication of flexible photosensors.[8] However, these materials are neither environmentally friendly nor chemically stable. Saran *et al.* suggested an inorganic (PbS quantum dot)/organic (phenyl-C61-butyric acid methyl ester) hybrid photosensor to improve the device performance.[9] Unfortunately, its photoresponsivity was unacceptably low at 0.051 A W^{-1}. According to recent reports, group III-nitride semiconductor materials have been considered as potential candidates for the fabrication of highly efficient optoelectronics operating in the wavelength window ranging from ultraviolet to near-infrared by controlling their composition.[10,11] The group III-nitride epitaxial film is typically grown on Si and sapphire substrates, but heteroepitaxial growth does not easily enable highly crystalline group III-nitride films to be grown due to the differences between the parameters of these materials such as their lattice constants and thermal expansion coefficients.[12,13] Furthermore, the fabrication of stretchable devices is additionally complicated by

---

Department of Electronic and Information Materials Engineering, Division of Advanced Materials Engineering, and Research Center of Advanced Materials Development, Jeonbuk National University, Jeonju 54896, Republic of Korea. E-mail: kjinsoo@jbnu.ac.kr

the inherently brittle characteristics of these materials. The use of group III-nitride nanowires (NWs) would be an alternative approach for overcoming this intrinsic limitation.[14] For example, Han *et al.* reported a stretchable photosensor fabricated with GaN NWs that operated from ultraviolet to visible wavelengths.[15] InN NWs are appropriate for use as light-absorbing media for stretchable photosensors operating at a wavelength of 1.3 μm because InN has a wide band gap from 0.6 to 1.1 eV, high electron mobility, and high saturation velocity.[16–18] Herein, we report highly efficient stretchable photosensors operating at the wavelength of 1.3 μm that exceeds the flexible characteristics for practical applications in attachable or wearable devices. The new photosensors incorporate InN NWs and graphene, which function as the light-absorbing medium and carrier channel, respectively. The stretchable photosensor was fabricated using the graphene/InN NWs/graphene structure (the so-called sandwich structure), in which InN NWs were randomly and horizontally embedded in the graphene layers. This structure was subsequently mounted on a pre-strained polyurethane (PU) substrate at strain levels of 10, 20, 30, 40, 50, and 60%. The device performance of the stretchable photosensors was assessed by measuring their photocurrent as a function of the light intensity and stretching condition. In addition, the effect of the external humidity and operation time on the device performances was evaluated.

Experimental methods

InN NWs were grown on a Si(111) substrate using a procedure known as the indium (In) pre-deposition method with plasma-assisted molecular-beam epitaxy. A schematic illustration of the formation of InN NWs using this method is shown in Fig. 1a. First, an *in situ* annealing process was carried out at 900 °C for 1 hour to remove the native oxide layer that naturally formed on the surface of Si(111) substrates (deoxidation process) before the growth of the InN NWs. After the deoxidation process, a nitridation process was implemented to form a thin film of SiN_x by exposing the Si(111) substrate to a N-plasma flux at a growth temperature of 800 °C. Thereafter, only In with a beam equivalent pressure of 4.2×10^{-8} torr was supplied for 6 s without the N-plasma to the SiN_x/Si(111) substrate to form In droplets to act as initial nucleation sites for the subsequent growth of the InN NWs. Because the bonding energy between In and N atoms is stronger than that between In and Si atoms, the SiN_x layer can promote the formation of In droplets.[19] As the final step, InN NWs were formed from the initial nucleation sites created by the In droplets by simultaneously providing In and N-plasma fluxes at a growth temperature of 500 °C and a group V/III ratio of 145 for 6 hours. Details of the growth conditions and the characterization of the InN NWs are provided in our previous paper.[19]

The structural properties of the InN NWs were analyzed using field-emission scanning electron microscopy (FE-SEM, Hitachi Su-70, installed in the Future Energy Convergence Core Center at Jeonbuk National University), double-crystal X-ray diffraction (DCXRD, Rigaku MAX-2500), and aberration-corrected transmission electron microscopy (TEM, Jeol JEM-ARM200F). Photoluminescence (PL) spectroscopy was used to investigate the optical properties of the InN NWs. The structural properties of graphene were analyzed by Raman spectroscopy (Renishaw inVia Reflex instrument). The characteristic current (*I*)–voltage (*V*) curves of the stretchable photo-

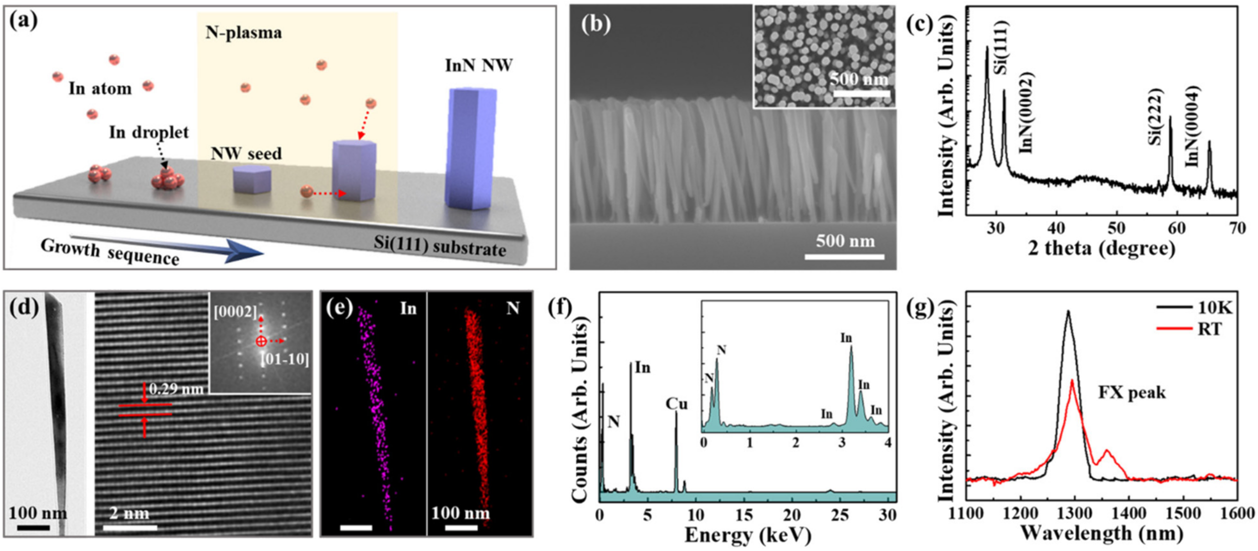

Fig. 1 (a) Schematic illustration of the formation of InN NWs using the In pre-deposition method. (b) Cross-sectional and plan-view (inset) FE-SEM images of the InN NWs. (c) DCXRD curve of the InN NWs. (d) TEM (left) and HR-TEM (right) images of an InN NW. Inset: SAED pattern. (e) EDS mapping images of the InN NW, showing the distribution of In (purple) and N (red). (f) EDS spectrum of the InN NWs, where the inset shows the expanded plot from 0 to 4 keV range. (g) PL spectra of the InN NWs measured at 10 K and RT.

sensors were recorded using a source meter (Keithley 2400). A xenon lamp (McScience, MAX-303) was used as a light source.

Results and discussion

Fig. 1b shows a cross-sectional FE-SEM image of the InN NWs formed on the Si(111) substrate. The inset shows a plan-view FE-SEM image of the InN NWs. From the FE-SEM images, the average length and diameter of the InN NWs were found to be 802 ± 3 and 62 ± 0.4 nm, respectively. The NW sizes were calculated using Image J software installed in the FE-SEM system. Fig. 1c shows the DCXRD rocking curve of the InN NWs formed on Si(111). The curve reveals four spectral peaks at 28.3, 31.2, 58.7, and 65.1°, which correspond to the crystalline signals of Si(111), InN(0002), Si(222), and InN(0004), respectively. The full-width at half-maximum (FWHM) values of the InN(0002) and InN(0004) peaks were calculated to be 0.35 and 0.33°, respectively. These values are smaller than those in previous reports, indicating that highly crystalline InN NWs with the wurtzite (WZ) crystal structure were formed.[20,21] Fig. 1d shows a transferred NW on a grid (left) and a bright-field high-resolution TEM (HR-TEM) image (right) of a single InN NW. The NW shows a slightly tapered shape, which is attributed to the increase in the probability of lateral migration rather than vertical migration of the In adatoms due to the nitrogen blocking effect. This result is consistent with that observed in the FE-SEM image. The HR-TEM image of the InN NW enabled the interplanar distance to be calculated as 0.29 nm, which corresponds well with the spacing of InN with the WZ crystal structure. In addition, stacking faults and defects, which are typically observed in Si-based group III–V compound-semiconductor NWs due to the differences in the parameters of these materials, were largely absent.[22,23] In our previous works, the stacking faults were rarely observed from the HR-TEM images and selective-area electron diffraction (SAED) patterns measured at three different positions of the InN NW along the vertical growth direction.[19] The inset in the HR-TEM image shows the SAED pattern. This pattern clearly shows that the [0002] and [01−10] growth directions originated from the InN NW with the WZ crystal structure,[24] and is consistent with the DCXRD rocking curve shown in Fig. 1c. In the electron-dispersive spectroscopy (EDS) mapping of the InN NW shown in Fig. 1e, In and N are uniformly distributed throughout the InN NW. Each map is displayed by the relative intensity scale, where purple and red colors represent In and N atoms, respectively. Fig. 1f shows the EDS spectrum of the InN NWs. The peak at 8 keV corresponds to the Cu element originating from the Cu plate. As shown in the inset of Fig. 1f, the InN NW only contains the expected elements, In and N. Fig. 1g shows the PL spectra of the InN NWs measured at 10 K and room temperature (RT). The excitation power was set to 3 mW cm^{-2}. A free-exciton (FX) peak measured at 10 K was observed at the wavelength of 1288 nm with a small FWHM value of 21 nm. The emission wavelength of the InN NWs in this work was significantly blue-shifted compared to those of the InN bulk or thin films that have been previously reported.[25–27] This result is attributed to the combined influence of the Burstein–Moss effect, in which the higher energy levels of the conduction band are occupied due to the considerable accumulation of surface electrons on the InN NWs, and the quantum confinement effect of the InN NWs.[28,29] Typically, it is quite difficult to observe the FX peak at RT, because a significant number of the photo-generated carriers are trapped in stacking faults that are commonly present inside Si-based group III–V NWs. This phenomenon results in insufficient radiative recombination and increased nonradiative recombination.[30] However, in this work, a strong FX peak was observed at the wavelength of 1297 nm with a small FWHM value of 25 nm at RT, indicating the formation of highly crystalline InN NWs. The valley observed around the wavelength of 1330 nm is associated with water absorption.[19]

Fig. 2a schematically illustrates the fabrication of stretchable photosensors using the InN NWs that are randomly and horizontally embedded in the graphene sandwich structure on the pre-strained PU substrate. The stretchable photosensors were fabricated by first separating the InN NWs from the Si(111) substrate using an ultrasonic mechanical process in which the InN NW samples with a size of 2 × 2 cm^2 were immersed in 2 mL of isopropyl alcohol (IPA), whereupon the InN NW/IPA solution was dispersed on the bottom graphene layer (step 1). Subsequently, the top graphene channel was formed by transferring single-layer graphene onto the InN NWs/graphene structure using a standard wet-transfer process (step 2). After the formation of the graphene/InN NWs/graphene sandwich structure, the Cu substrate was etched in an ammonium persulfate (AP) solution with a concentration of 1 molar prepared by adding AP to deionized water. Finally, the stretchable photosensors were fabricated by transferring the graphene/InN NWs/graphene sandwich structure onto the pre-strained PU substrates with different strains defined as 100 × ($\Delta L/L$), where ΔL and L are the relative change in the length after stretching and the initial length of the PU substrate, respectively. The stretchable photosensors were fabricated with the pre-strain levels of 0, 10, 20, 30, 40, 50, and 60%. Fig. 2b shows the Raman spectrum of the graphene layer. To prevent the graphene from incurring mechanical damage during the measurement, the excitation power of the laser with an operating wavelength of 532 nm was set to the low value of 1 mW. The intense G and 2D peaks observed at 1586.6 and 2675.5 cm^{-1}, respectively, are consistent with the values for the excitation laser energy of 2.33 eV (532 nm).[31,32] The ratio of the intensity of the 2D and G peaks (I_{2D}/I_G) was calculated to be 2.12, which is comparable to previously reported values for single-layer graphene.[33,34] The FWHM values of the G and 2D peaks were calculated to be 21 and 32 cm^{-1}, respectively. Neumann *et al.* reported that the shape and FWHM value of the 2D peak were largely affected by the strain resulting from the lattice deformation during the graphene transfer process.[35] For example, when strain is applied to graphene, the shape of the 2D peak becomes asymmetric and its FWHM increases. However, in our work, the graphene gave rise to a

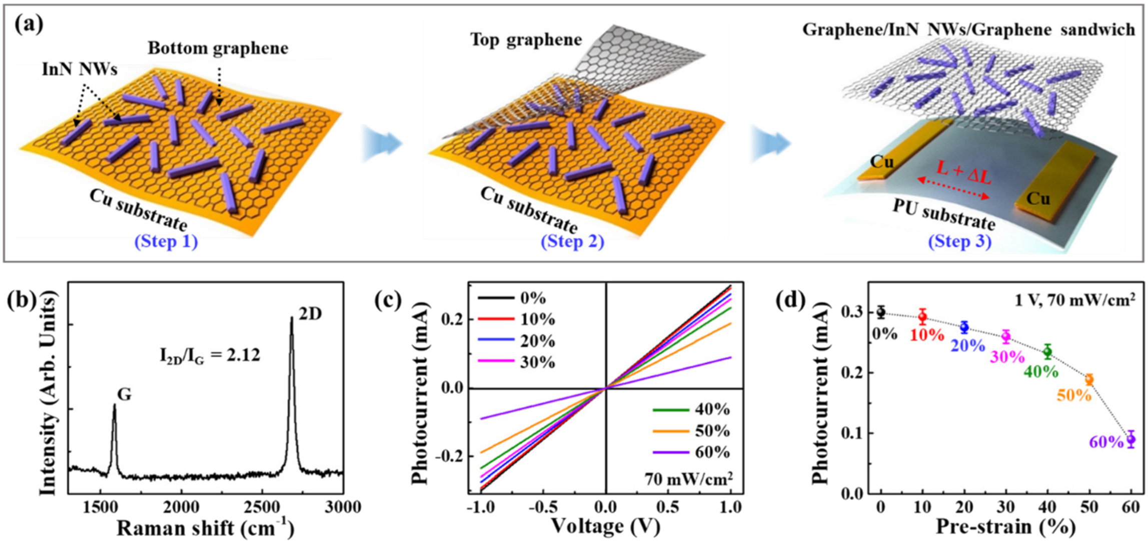

Fig. 2 (a) Fabrication process of the stretchable photosensor with InN NWs and graphene. (b) Raman spectrum of graphene used as the carrier channel. (c) Characteristic *I*–*V* curves for the stretchable InN-NW photosensors depending on the pre-strain values at the light intensity of 70 mW cm^{-2}. (d) Summary of the dependence of the photocurrent on the degree of pre-strain of the PU substrate.

symmetrical 2D peak with a small FWHM value, indicating that the effect of the strain caused by the deformation of the graphene lattice is negligible. To optimize the device performance of the stretchable photosensor according to the degree of pre-strain, devices with various degrees of pre-strain were prepared, and their photocurrents were measured in the released state at the light intensity of 70 mW cm^{-2} and voltage of 1 V. The characteristic *I*–*V* curves of the stretchable InN-NW photosensors in the released state, measured by varying the degree of pre-strain, and a summary of the dependence of the photocurrent on the degree of the pre-strain of the PU substrate are shown in Fig. 2c and d, respectively. The photocurrent was calculated by subtracting the dark current from the light current. The decrease in the photocurrent from 0.31 to 0.19 mA with an increasing degree of pre-strain from 0 to 50% can be explained by the scattering effect of the charge carriers in the ripple-structured graphene channels.[8] As the degree of pre-strain further increased to 60%, the intensive charge carrier scattering and mechanical damage to the graphene channels due to the excessive strain applied to the PU substrate drastically weakened the photocurrent to 0.09 mA. Considering these results, in subsequent tests, the performance of the photosensor fabricated by applying pre-strain of 50% was evaluated in greater detail under various conditions.

The characteristic *I*–*V* curves of the stretchable InN-NW photosensor in the released state, measured by varying the light intensity, and a summary of the dependence of the photocurrent and photoresponsivity on the light intensity, are shown in Fig. 3a and b, respectively. At the light intensity of 70 mW cm^{-2}, the photocurrent was found to be 0.19 mA, which is significantly higher than the values measured in previous studies on stretchable photosensors. For example, Li *et al.* reported a stretchable photosensor fabricated with SnO_2/polydimethylsiloxane, but the photocurrent was extremely weak at 120 pA.[36] Keeping in mind the difficulty of fabricating a highly efficient stretchable photosensor using inorganic semiconductors due to their inherent brittleness, it is noteworthy that the strong photocurrent of the photosensor in this work was obtained using inorganic InN NWs. The strong photocurrents produced by the photosensor can be explained by the large number of photo-generated carriers originating from the highly crystalline InN NWs and the high carrier mobility of graphene. The photoresponsivities at the applied voltage of 1 V and the light intensities of 10, 30, 50, and 70 mW cm^{-2} were calculated to be 4.60, 4.32, 3.54, and 2.73 A W^{-1}, respectively. Even though the photocurrent strengthens as the light intensity increases, the carrier scattering effect caused by the increase in the thermal energy of the incident light increases and consequently lowers the photoresponsivities.[37] Fig. 3c shows the characteristic *I*–*V* curves of the stretchable InN-NW photosensor as a function of the degree of strain, measured at the light intensity of 70 mW cm^{-2}. The strain applied to the device was defined as the length of the stretched device divided by the length of the device in its initial state. The photocurrents at the strain of 10, 20, 30, 40, and 50% were found to be 0.187, 0.177, 0.172, 0.159, and 0.144 mA, respectively. As the strain increases, the photocurrents weaken slightly because of the decrease in photon absorption due to internal reflection and the quantum mechanical tunneling probability of carriers in the graphene sandwich structure. However, the extent to which the device performance deteriorated due to the strain applied to the device was much smaller for our stretchable InN-NW photosensors compared to previous results.[8,38] For example, Chiang *et al.* reported that the photocurrent produced by stretchable photosensors based on graphene quantum dots weakened by

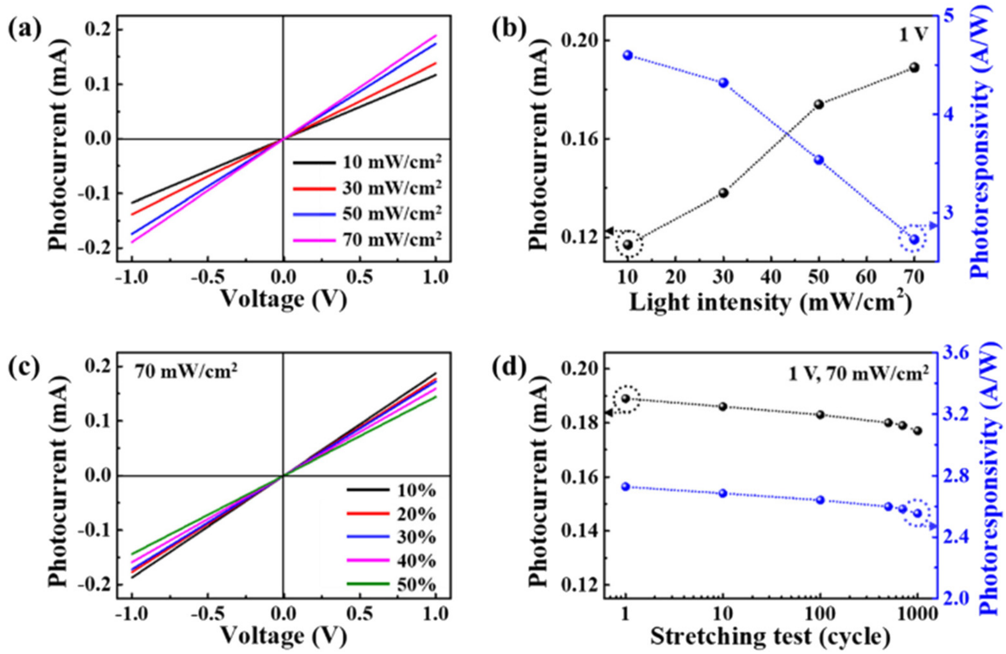

Fig. 3 (a) Characteristic *I–V* curves for the stretchable InN-NW photosensor at various light intensities. (b) Summary of the dependence of the photocurrent and photoresponsivity on the light intensity. (c) Characteristic *I–V* curves for the photosensor for the indicated strain values. (d) Summary of the photocurrent of the photosensor for the indicated number of stretching cycles.

80% as the degree of strain increased to 25%.[38] To evaluate the durability of the stretchable photosensor, cyclic-stretching tests were carried out at a strain level of 50%. The photocurrents and photoresponsivities of the stretchable photosensor subjected to various numbers of cycles of stretching are shown in Fig. 3d. The photocurrents (photoresponsivities) of the stretchable InN-NW photosensor subjected to 1, 10, 100, 500, 700, and 1000 cycles of stretching were found to be 0.189 (2.728), 0.186 (2.685), 0.183 (2.641), 0.180 (2.598) 0.179 (2.583), and 0.177 mA (2.554 A W^{-1}), respectively. After 1000 cycles of stretching, although the photocurrent and photoresponsivity deteriorated slightly, the extent of degradation of the device performance is sufficiently low to ignore. This result indicates that the fabricated stretchable photosensor has reliable mechanical durability.

Because attachable or wearable devices are inevitably exposed to ambient humidity, it is important to develop photosensors that operate reliably in humid environments for their practical applications. To evaluate the humidity stability, the photocurrent was measured by varying the external relative humidity using a mass-flow controller (i-300CV-S4) in a humidity chamber under an applied voltage of 1 V and light intensity of 70 mW cm^{-2} and the results are shown in Fig. 4a. The photocurrents at the relative humidity levels of 20, 35, 50, 65, and 80% were found to be 0.189, 0.188, 0.188, 0.187, and 0.186 mA, respectively. The very limited degradation of the photocurrent at higher relative humidity levels indicated that our stretchable photosensors are significantly stable under humid conditions. The photocurrent generated by the stretchable photosensor was monitored for an extended period of

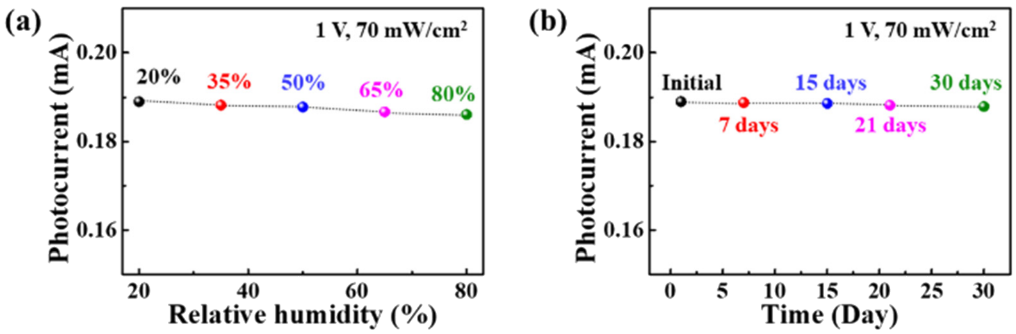

Fig. 4 (a) Dependence of the photocurrent of the photosensor on the relative humidity. (b) Photocurrent of the photosensor: measured immediately, and 7, 15, 21, and 30 days after device fabrication.

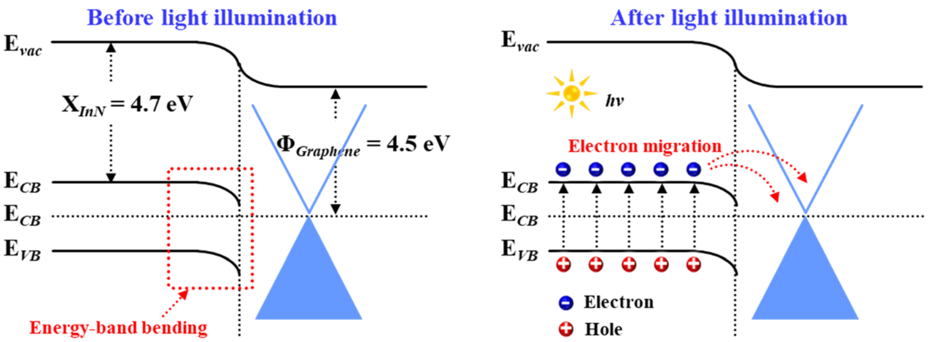

Fig. 5 Schematic illustration of the operational mechanism of the photosensor.

time to assess the operating stability of the device, and the results are plotted in Fig. 4b. The photocurrent measured immediately, and 7, 15, 21, and 30 days after the device fabrication was 0.189, 0.188, 0.187, 0.187, and 0.187 mA, respectively. These results indicate that the photocurrent is negligibly degraded over time, and therefore that our stretchable photosensor is capable of stable long-term operation.

Fig. 5 graphically illustrates the energy-band structure to explain the operational mechanism of the stretchable photosensor. Before illumination with light, the difference between the electron affinity of InN NWs (X_{InN}) and the work function of graphene (Φ_{Graphene}) causes the energy band of the InN-NW surface to bend downward such that it matches the Fermi level at the hetero-interface between the InN NWs and graphene. After illumination with light, the alignment of the energy band between the InN NWs and graphene enables the photoelectrons generated at the InN NWs to move to the graphene. These electrons migrate to the electrodes through the graphene channels and contribute to the photocurrent without significant loss.[39]

Conclusions

In conclusion, we successfully fabricated a stretchable photosensor based on InN NWs and graphene on a pre-strained PU substrate. The photosensor operates at the wavelength of 1.3 μm. In the released state, the stretchable InN-NW photosensor prepared on 50% pre-strained PU generated a photocurrent of 0.189 mA under light intensity of 70 mW cm^{-2} and an applied voltage of 1 V. In the 50% strained state, the photocurrent of the stretchable InN-NW photosensor was found to be 0.144 mA. This value corresponds to 76.2% of that obtained in the released state, indicating that our stretchable InN-NW photosensor in this work delivers device performance superior to previously reported results. The significant improvement in the device performance can be explained by the high crystallinity of the InN NWs and the conformal contact between the InN NWs and graphene, which can facilitate carrier transport and reduce charge recombination due to the high carrier mobility of graphene. A systematic analysis of the stretchable photosensor to determine the effect of the light intensity, number of stretching cycles, relative humidity, and operation time indicated that the device performance could be considered sufficient for real-life practical application.

Author contributions

J.S.K. designed the research project and supervised the experiments. J.S., S.N., S.J., S.K., and Y.L. performed the experiments and analyzed the data. J.S.K. and J.S. wrote the paper, which was discussed by all the authors.

Data availability

The data that support the findings of this study are available from the corresponding author (Jin Soo Kim) upon reasonable request.

Conflicts of interest

There are no conflicts to declare.

Acknowledgements

This work was supported in part by the National Research Foundation of Korea (NRF) funded by the Ministry of Education (No. 2023R1A2C1005913) and by the Civil-Military Technology Cooperation Program (No. 19-CM-BD-05).

References

1 O. A. Kozyreva, Y. V. Solo'ev, I. S. Polukhin, A. K. Mikhailov, G. A. Mikhailovskiy, M. A. Odnoblyudov, E. Z. Gareev, E. S. Kolodeznyi, I. I. Novikov, L. Y. Karachinsky, A. Y. Egorov and V. E. Bougrov, High-speed 1.3-1.5 μm InGaAs/InP PIN photodetector for microwave photonics, *J. Phys.: Conf. Ser.*, 2017, **917**, 052029.

2 H. Xu, J. Liu, J. Zhang, G. Zhou, N. Luo and N. Zhao, Flexible organic/inorganic hybrid near-infrared photo-

plethysmogram sensor for cardiovascular monitoring, *Adv. Mater.*, 2017, **29**, 1700975.

3 N. Balkan, A. Erol, F. Sarcan, L. F. F. Al-Ghuraibawi and M. S. Nordin, Dilute nitride resonant cavity enhanced photodetector with internal gain for the λ~1.3 μm optical communications window, *Superlattices Microstruct.*, 2015, **86**, 467.

4 J. Rani, P. Chauhan and R. Tripathi, Li-Fi (Light Fidelity)-The future technology in wireless communication, *Int. J. Appl. Eng. Res.*, 2012, **7**, 0973.

5 R. Karthika and S. Balakrishnan, Wireless communication using Li-Fi technology, *SSRG-IJECE*, 2015, **2**, 32.

6 J. Shin, H. Yang, S. Noh, S. Han and J. S. Kim, Flexible 1.3 μm photodetector fabricated with InN nanowires and graphene on overhead projector transparency sheet, *Nanoscale*, 2022, **14**, 10793.

7 C. Lee, H. Kim and Y. Kim, Short-wave infrared organic phototransistors with strong infrared-absorbing polytriarylamine by electron-transfer doping, *npj Flexible Electron.*, 2021, **5**, 10.

8 K. P. Bera, G. Haider, M. Usman, P. K. Roy, H.-I. Lin, Y.-M. Liao, C. R. P. Inbaraj, Y.-R. Liou, M. Kataria, K.-L. Lu and Y.-F. Chen, Trapped photons induced ultrahigh external quantum efficiency and photoresponsivity in hybrid graphene/metal-organic framework broadband wearable photodetectors, *Adv. Funct. Mater.*, 2018, **28**, 1804802.

9 R. Saran and R. J. Curry, Lead sulphide nanocrystal photodetector technologies, *Nat. Photonics*, 2016, **10**, 81.

10 S. Noh, J. Song, S. Han, J. Shin, Y.-T. Yu and J. S. Kim, Drastic improvement in photoelectrochemical water splitting performance over prolonged reaction time using new carrier-guiding semiconductor nanostructures, *J. Mater. Chem. A*, 2022, **10**, 9821.

11 L. Caccamo, J. Harmann, C. Fàbrega, S. Estradé, G. Lilienkamp, J. D. Prades, M. W. G. Hoffmann, J. Ledig, A. Wagner, X. Wang, L. Lopez-Conesa, F. Peiró, J. M. Rebled, H.-H. Wehmann, W. Daum, H. Shen and A. Waag, Band engineered epitaxial 3D GaN-InGaN core-shell rod arrays as an advanced photoanode for visible-light-driven water splitting, *ACS Appl. Mater. Interfaces*, 2014, **6**, 2235.

12 S. Weiszer, A. Zeidler, M. D. L. Mata and M. Stutzmann, Growth of self-assembled and position controlled InN nanowires on Si(111) by molecular beam epitaxy, *J. Cryst. Growth*, 2019, **510**, 56.

13 S. Han, I. Choi, J. Song, C.-R. Lee, I.-W. Cho, M.-Y. Ryu and J. S. Kim, Structural and optical properties of GaN nanowires formed on Si(111), *Appl. Sci. Converg. Technol.*, 2018, **10**, 38173.

14 S. Han, S.-K. Lee, I. Choi, J. Song, C.-R. Lee, K. Kim, M.-Y. Ryu, K.-U. Jeong and J. S. Kim, Highly efficient and flexible photosensors with GaN nanowires horizontally embedded in a graphene sandwich channel, *ACS Appl. Mater. Interfaces*, 2018, **10**, 38173.

15 S. Han, S. Noh, J.-W. Kim, C.-R. Lee, S.-K. Lee and J. S. Kim, Stretchable inorganic GaN-nanowire photosensor with high photocurrent and photoresponsivity. ACS Appl Mater Interfaces, *ACS Appl. Mater. Interfaces*, 2021, **13**, 22728.

16 T. Inushima, V. V. Mamutin, V. A. Vekshin, S. V. Ivanov, T. Sakon, M. Motokawa and S. Ohoya, Physical properties of InN with the band gap energy of 1.1 eV, *J. Cryst. Growth*, 2001, **227**, 481.

17 Y. Nanishi, Y. Saito and T. Yamaguchi, RF-molecular beam epitaxy growth and properties of InN and related alloys, *Jpn. J. Appl. Phys.*, 2003, **42**, 2549.

18 M. Higashiwaki and T. Matsui, Estimation of band-gap energy of intrinsic InN from photoluminescence properties of undoped and Si-doped InN films grown by plasma-assisted molecular-beam epitaxy, *J. Cryst. Growth*, 2004, **269**, 162.

19 J. Shin, S. Noh, J. Lee, J. Oh, M.-Y. Ryu and J. S. Kim, Structural and optical properties of InN nanowires formed on Si(111), *Appl. Sci. Converg. Technol.*, 2022, **31**, 141.

20 S. Feng, J. Tan, B. Li, H. Song, Z. Wu and X. Chen, Nitridation effects of Si(111) substrate surface on InN nanorods grown by plasma-assisted molecular beam epitaxy, *J. Alloys Compd.*, 2015, **621**, 232.

21 M. Zeghouane, G. Avit, T. W. Cornelius, D. Salomon, Y. André, C. Bougerol, T. Taliercio, A. M. Sado, P. Ferret, D. Castelluci, E. Gil, E. Tournié, O. Thomas and A. Trassoudaine, Selective growth of ordered hexagonal InN nanorods, *CrstEngComm*, 2019, **21**, 2702.

22 S. Eftychis, J. Kruse, T. Koukoula, T. Kehagias, P. Komninou, A. Adikimenakis, K. Tsagaraki, M. Androulidaki, P. Tzanetakis, E. Iliopoulos and A. Georgakilas, Understanding the effects of Si(111) nitridation on the spontaneous growth and properties of GaN nanowires, *J. Cryst. Growth*, 2016, **442**, 8.

23 R. S. Chen, H. Y. Tsai, C. H. Chan, Y. S. Huang, Y. T. Chen, K. H. Chen and L. C. Chen, Comparison of CVD- and MBE-grown GaN nanowires: Crystallinity, photoluminescence, and photoconductivity, *J. Electron. Mater.*, 2015, **44**, 177.

24 H. J. Joyce, J. Wong-Leung, Q. Gao, H. H. Tan and C. Jagadish, Phase perfection in zinc blende and wurtzite III-V nanowires using basic growth parameters, *Nano Lett.*, 2010, **10**, 908.

25 E. A. Anyebe, Q. Zhuang, M. Kesaria and A. Krier, The structural evolution of InN nanorods to microstructures on Si(111) by molecular beam epitaxy, *Semicond. Sci. Technol.*, 2014, **29**, 085010.

26 R. Intartaglia, B. Maleyre, S. Ruffenach, O. Briot, T. Taliercio and B. Gil, Radiative and nonradiative recombination processes in InN films grown by metal organic chemical vapor deposition, *Appl. Phys. Lett.*, 2005, **86**, 142104.

27 W. Walukiewicz, J. W. Ager III, K. M. Yu, Z. Liliental-Weber, J. Wu, S. X. Li, R. E. Jones and J. D. Denlinger, Structure and electronic properties of InN and In-rich group III-nitride alloys, *J. Phys. D: Appl. Phys.*, 2006, **39**, R83.

28 W. C. Ke, C. P. Fu, C. Y. Chen, L. Lee, C. S. Ku, W. C. Chou, W.-H. Chang, M. C. Lee, W. K. Chen, W. J. Lin and

Y. C. Cheng, Photoluminescence properties of self-assembled InN dots embedded in GaN grown by metal organic vapor phase epitaxy, *Appl. Phys. Lett.*, 2006, **88**, 191913.

29 K. K. Madapu and S. Dhara, Effect of strain relaxation and the Burstein-Moss energy shift on the optical properties of InN films grown in the self-seeded catalytic process, *CrystEngComm*, 2016, **18**, 3114.

30 T. Auzelle, B. Haas, M. D. Hertog, J.-L. Rouvière, B. Daudin and B. Gayral, Attribution of the 3.45 eV GaN nanowires luminescence to inversion domain boundaries, *Appl. Phys. Lett.*, 2015, **107**, 051904.

31 E. J. Heller, Y. Yang, L. Kocia, W. Chen, S. Fang, M. Borunda and E. Kaxiras, Theory of graphene raman scattering, *ACS Nano*, 2016, **10**, 2803.

32 A. Armano, G. Buscarino, F. Messina, A. Sciortino, M. Cannas, F. M. Gelardi, F. Giannazzo, E. Schilirò and S. Agnello, Dynamic modification of Fermi energy in single-layer graphene by photoinduced electron transfer from carbon dots, *Nanomaterials*, 2020, **10**, 528.

33 A. C. Ferrari, J. C. Meyer, V. Scardaci, C. Casiraghi, M. Lazzeri, F. Mauri, S. Piscanec, D. Jiang, K. S. Novoselov, S. Roth and A. K. Geim, Raman spectrum of graphene and graphene layers, *Phys. Rev. Lett.*, 2006, **97**, 187401.

34 I. Calizo, I. Begenari, M. Rahman, G. Liu and A. A. Balandin, Ultraviolet Raman microscopy of single and multilayer graphene, *J. Appl. Phys.*, 2009, **106**, 043509.

35 C. Neumann, S. Reichardt, M. Drögeler, L. Banszerus, M. Schmitz, K. Watanabe, T. Taniguchi, F. Mauri, B. Beschoten, S. V. Rotkin and C. Stampfer, Raman spectroscopy as probe of nanometre-scale strain variations in graphene, *Nat. Commun.*, 2015, **6**, 8429.

36 L. Li, Z. Lou, H. Chen, R. Shi and G. Shen, Stretchable SnO_2-CdS interlaced-nanowire film ultraviolet photodetectors, *Sci. China Mater.*, 2019, **62**, 1139.

37 P. Yu, X. Yu, W. Lu, H. Lin, L. Sun, K. Du, F. Liu, W. Fu, Q. Zeng, Z. Shen, C. Jin, Q. L. Wang and Z. Liu, Fast photoresponse from 1T tin diselenide atomic layers, *Adv. Funct. Mater.*, 2016, **26**, 137.

38 C.-W. Chiang, G. Haider, W.-C. Tan, Y.-R. Liou, Y.-C. Lai, R. Ravindranath, H.-T. Chang and Y.-F. Chen, Highly stretchable and sensitive photodetectors based on hybrid graphene and graphene quantum dots, *ACS Appl. Mater. Interfaces*, 2016, **8**, 466.

39 S. Han, I. Choi, C.-R. Lee, K.-U. Jeong, S.-K. Lee and J. S. Kim, Fast response characteristics of flexible ultraviolet photosensors with GaN nanowires and graphene, *ACS Appl. Mater. Interfaces*, 2019, **12**, 970.